CrystEngComm

PAPER

View Article Online
View Journal | View Issue

Cite this: *CrystEngComm*, 2024, **26**, 4804

Received 28th June 2024,
Accepted 8th August 2024

DOI: 10.1039/d4ce00655k

rsc.li/crystengcomm

Bimetallic metal–organic framework-derived cobalt selenide-based composites as bifunctional electrocatalysts for both hydrogen evolution and mono-alcohol oxidation†

Lei Hu, *[a] Peng Zhong,[a] Jie Zhu,[a] Jiacheng Wang,[a] Yuchen Zheng,[a] Xiaoming Lin, [c] Yuyang Zhang[a] and Hao Yang *[b]

It is essential for energy-saving hydrogen production that an individual catalyst integrates the dual centers of mono-alcohol oxidation and hydrogen evolution. Nevertheless, such integration is thwarted for practical applications owing to insufficient active centers on catalysts. Herein, we created a combination of copper-infused $Co_{0.85}Se$ enclosed in an N-doped carbon structure (namely Cu-$Co_{0.85}$Se@NC), allowing for controlled integration of Cu atoms into $Co_{0.85}Se$ to adjust the electronic configuration. The electronic modulation induces the generation of well-defined dual active sites, which could optimize mono-alcohol/water adsorption behavior, thus achieving excellent mono-alcohol oxidation and hydrogen evolution properties. Specifically, the activity order of mono-alcohol oxidation on the Cu-$Co_{0.85}$Se@NC electrode is methanol > ethanol > isopropanol > *n*-propanol. Moreover, the necessary voltage for electrolyzing water with methanol assistance is clearly lower than that for regular water electrolysis. This work exhibits a promising strategy for developing energy-saving hydrogen production applications and corresponding high-activity catalysts.

1. Introduction

A major obstacle is the tight coupling of the energy-inefficient and slow anodic oxygen evolution reaction (OER) with the cathodic hydrogen generation process, leading to a significant reduction in electrolytic water efficiency.[1,2] The substitution of OER with a thermodynamically more advantageous organic oxidation reaction decreases the generation of detrimental reactive oxygen species, reduces the potential demand for the electrocatalytic reaction, and improves the efficiency of hydrogen production.[3–5] Recently, alcohol-assisted hydrogen generation (or electrochemical alcohol reforming) at a potential lower than that demanded for traditional water splitting has been investigated.[6–9] It has been shown that the selection of alcohols has a great influence on the overall electrocatalytic properties.[10,11] A simple anodic oxidation process that demonstrates better kinetics and thermodynamics than OER should be used to expand flexibility and determine the practical capabilities of this innovative strategy. Meanwhile, the environmental and cost aspects of anodic substrates should also be investigated. Therefore, biomass and its derivatives (including methanol, ethanol, *n*-propanol, and isopropanol) are up-and-coming candidates for alcohol-assisted hydrogen generation. Besides, high concentrations of alcohol molecules contribute to the generation of high current density, but excessive concentrations can also reduce the active sites on the electrode, thereby reducing the electrocatalytic performance.[12,13] Nevertheless, to our knowledge, no investigations on the influence of mono-alcohol oxidation reactions (M-AOR) using alcohols with different concentrations as additives have been reported.

On the other hand, most of the as-synthesized catalysts do not exhibit excellent bifunctionality for both the hydrogen evolution reaction (HER) and M-AOR due to the incompatibility of active centers in matching catalytic processes. Transition metal selenide (TMSe) catalysts, especially cobalt selenide, exhibit excellent activity in HER, but their M-AOR performance is unsatisfactory.[14–18] In view of this, modification methods have been developed to boost the electrocatalytic properties of cobalt selenide-based catalysts for alcohol-assisted hydrogen generation.[19–21] The effective strategy concerns amalgamating a second metal into the cobalt selenide to fabricate an elaborate

---

[a] *School of Chemical and Environmental Engineering, Anhui Polytechnic University, Wuhu 241000, China. E-mail: hulei@ahpu.edu.cn*

[b] *School of Chemistry & Chemical Engineering, Guangxi University, Nanning 530004, China. E-mail: yanghao@gxu.edu.cn*

[c] *School of Chemistry, South China Normal University, Guangzhou 510006, China*

† Electronic supplementary information (ESI) available. See DOI: **https://doi.org/10.1039/d4ce00655k**

intermetallic catalyst.[22,23] The coordination structure of the cobalt is altered after generating an intermetallic catalyst, resulting in a change in the electronic structures of both metals.[24,25] Besides, electrons are partially transferred to the atom with lower orbital energy, subsequently shifting the d-band center relative to the Fermi energy level to change the adsorption behaviors of substrates, effectively improving the catalysts' activity.[26] Specifically, heterometallic copper can promote the Volmer step in alkaline media by fixing oxygen atoms in water molecules while also regulating the electronic structure of cobalt selenide and thus optimizing its adsorption on substrate molecules (or intermediates).[27] Therefore, it is logical to speculate that introducing heterometallic copper into cobalt selenide may exhibit superior catalytic performance towards HER and M-AOR by integrating the excellent features of each constituent.

Herein, a copper-doped cobalt selenide bifunctional catalyst (namely Cu-$Co_{0.85}$Se@NC) was fabricated for water electrolysis. Optimizing the electronic environment through heterometallic doping is an effective approach to enhancing the intrinsic activity of the catalyst. Besides, the oxidation reaction of methanol displays high activity on the Cu-$Co_{0.85}$Se@NC electrode. However, the oxidation of ethanol, isopropanol, and *n*-propanol depicts a relatively low activity. Significantly, utilizing the Cu-$Co_{0.85}$Se@NC bifunctional electrocatalysts for both cathode and anode resulted in a two-electrode methanol oxidation-assisted hybrid electrolyzer requiring only 1.46 V cell potential to reach 10 mA cm^{-2}, a reduction of 0.30 V compared to the traditional electrolyzer (1.76 V).

2. Experimental

2.1 Synthesis of bimetallic CuCo-MOF

2.7 mmol (0.7857 g) of $Co(NO_3)_2 \cdot 6H_2O$, 2.7 mmol (0.6523 g) of $Cu(NO_3)_2 \cdot 3H_2O$, and 44 mmol (4.2297 g) of 2-methylimidazole were dissolved in 120 mL of ultrapure water to produce a homogeneous solution. Lavender powder (namely CuCo-MOF) was obtained after three rounds of filtering and washing with methanol. Similarly, CuCo-MOF-1 was fabricated by mixing 3.6 mmol (1.0477 g) of $Co(NO_3)_2 \cdot 6H_2O$ with 1.8 mmol (0.4349 g) of $Cu(NO_3)_2 \cdot 3H_2O$, whereas CuCo-MOF-2 was synthesized with 1.8 mmol (0.5238 g) of $Co(NO_3)_2 \cdot 6H_2O$ and 3.6 mmol (0.8698 g) of $Cu(NO_3)_2 \cdot 3H_2O$. Additionally, a monometallic Co-MOF was synthesized using a comparable approach that did not involve the addition of $Cu(NO_3)_2 \cdot 3H_2O$.

2.2 Synthesis of Cu-$Co_{0.85}$Se@NC

Two positions in a crucible were filled with 400 mg of selenium powder and 200 mg of CuCo-MOF, with the selenium powder placed upstream of the furnace. The powders were calcined at 700 °C for 3 hours in an argon environment to fabricate the desirable products (namely Cu-$Co_{0.85}$Se@NC). Similarly, $Co_{0.85}$Se@NC, Cu-$Co_{0.85}$Se@NC-1, and Cu-$Co_{0.85}$Se@NC-2 were also fabricated under the same conditions using Co-MOF, CuCo-MOF-1 and CuCo-MOF-2 precursors.

2.3 Characterization

Scanning electron microscopy (SEM, Zeiss sigma300), transmission electron microscopy (TEM, FEI Tecnai F20), X-ray photoelectron spectroscopy (XPS, Thermo VG ESCALab250), X-ray diffraction (XRD, D8 ADVANCE) and Raman spectroscopy (Renishaw inVia) were used to analyze the morphology, structure and composition of the materials produced.

2.4 Electrochemical measurements

Electrochemical measurements were carried out on an electrochemical workstation (Chenhua, CHI 760E). Measurements of OER, M-AOR, and HER were conducted using a standard three-electrode setup. Particularly, the working electrode utilized a cobalt selenide nanocomposite, while the reference electrode was an Ag/AgCl electrode, and the counter electrode was a carbon rod. The electrolyte was created by combining 1 M KOH with varying amounts of alcohol solvent. The electrochemically active surface area (ECSA) of the electrocatalysts was calculated based on double-layer capacitance using CV measurements within a non-faradaic range at different scan rates. A symmetrical two-electrode electrochemical system was used to conduct the water electrolysis experiment.

3. Results and discussion

Fig. 1a displays the synthetic procedure for the cube-like composite material. Firstly, bimetallic CuCo-MOF nanocubes are synthesized through a room-temperature coprecipitation process. A solution containing copper nitrate, cobalt nitrate,

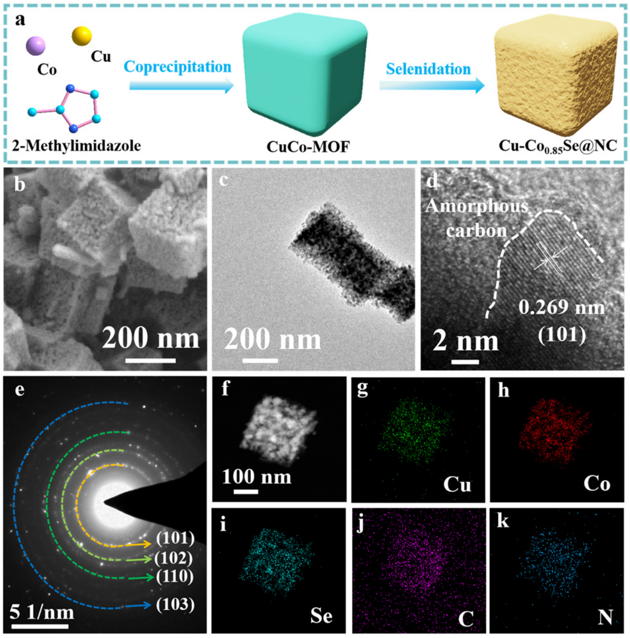

Fig. 1 (a) Synthesis route of the Cu-$Co_{0.85}$Se@NC composite. (b) SEM, (c) TEM, and (d) HR-TEM images of Cu-$Co_{0.85}$Se@NC composite. (e) SAED pattern of Cu-Co0.$_{85}$Se@NC composite. (f–k) EDS elemental mapping of Cu-$Co_{0.85}$Se@NC composite.

and 2-methylimidazole was prepared by dissolving them in ultrapure water. The resulting mixture was stirred for 1 hour to create the bimetallic CuCo-MOF precursor. SEM images reveal that the CuCo-MOF samples produced have a nanocubic shape and a sleek exterior (Fig. S1†). Subsequently, the obtained CuCo-MOF was annealed together with selenium powder to synthesize copper-doped $Co_{0.85}Se$ and nitrogen-doped carbon nanocomposites (denoted as Cu-$Co_{0.85}Se$@NC). The SEM image in Fig. 1b shows the rough surface and successful creation of a porous nanoarchitecture for Cu-$Co_{0.85}Se$@NC. Fig. 1c demonstrates that even after the selenidation process, the Cu-$Co_{0.85}Se$@NC composites retained the nanocubic structure of the CuCo-MOF precursor and consisted of uniformly arranged ultrafine nanogranules. The high-resolution transmission electron microscopy (HR-TEM) image (Fig. 1d) taken at the Cu-$Co_{0.85}Se$@NC interface showed a lattice spacing of 0.269 nm, corresponding to the (101) plane of Cu-$Co_{0.85}Se$. Besides, the TEM image illustrates well-dispersed Cu-$Co_{0.85}Se$ nanogranules in an amorphous carbon matrix (Fig. S2†). Fig. 1e displays the selected area electron diffraction (SAED) pattern of Cu-$Co_{0.85}Se$@NC, showing identifiable diffraction rings including (101), (102), (110), and (103). The energy dispersive spectrometer (EDS) mapping results in Fig. 1f–k illustrate the presence of Cu, Co, Se, C, and N elements in the hybrid material, indicating the successful integration of Cu into $Co_{0.85}Se$.

The XRD pattern in Fig. S3† shows that the Co-MOF and CuCo-MOF crystals were successfully prepared, and the addition of heterometallic Cu did not disrupt the Co-MOF structure.[28] The Co-MOF (Co(mIM)$_2$, CSD code GITTOT) corresponds to the structure reported by the Yaghi group.[29] Besides, $Co_{0.85}Se$@NC and Cu-$Co_{0.85}Se$@NC were also analyzed using XRD. With the exception of carbon, the diffraction patterns of both samples match those of standard $Co_{0.85}Se$ (JCPDS no. 52-1008). The enlarged region around positions (102) and (101) revealed a shift of the diffraction peaks towards a lower 2θ value, suggesting that larger Cu atoms had replaced smaller Co atoms (Fig. 2a–d).[30] The smaller radius of Co makes the Co–Se bond stronger than the Cu–Se bond. This means that Cu–Se bonds are more easily broken during the high-temperature synthesis process, resulting in the inability to obtain the copper selenide phase.[31] XPS analysis was performed to determine the chemical makeup and electronic configurations of the elements present in $Co_{0.85}Se$@NC and Cu-$Co_{0.85}Se$@NC. The survey spectrum in Fig. 2e confirmed the presence of Co, N, C, and Se in both composite materials, with Cu elements also being detected in Cu-$Co_{0.85}Se$@NC (Fig. S4†). Inductively coupled plasma optical emission spectroscopy (ICP-OES) testing showed that the atomic ratio of cobalt and copper in the Cu-$Co_{0.85}Se$@NC material was approximately 1 : 1, which is consistent with the results of XPS. Fig. 2f displays the Co 2p spectrum for both $Co_{0.85}Se$@NC and

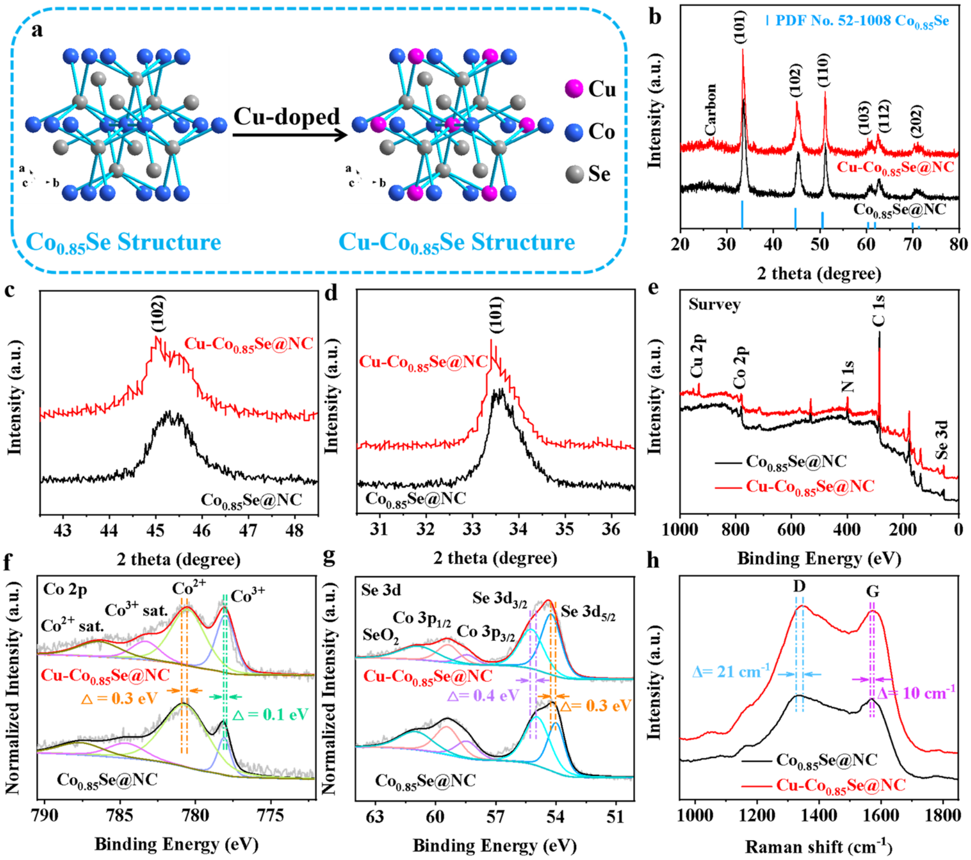

Fig. 2 (a) Schematic diagram of the copper-doped $Co_{0.85}Se$ structure. (b–d) XRD pattern of $Co_{0.85}Se$@NC and Cu-$Co_{0.85}Se$@NC. (e) Survey, (f) Co 2p, (g) Se 3d of $Co_{0.85}Se$@NC and Cu-$Co_{0.85}Se$@NC. (h) Raman spectra of $Co_{0.85}Se$@NC and Cu-$Co_{0.85}Se$@NC.

Cu-Co$_{0.85}$Se@NC, indicating that these composites consist of two distinct peaks representing Co^{3+} and Co^{2+}, along with two minor satellite peaks.[32,33] The binding energy of Co^{3+} and Co^{2+} in Cu-Co$_{0.85}$Se@NC depicts a negative shift, indicating greater electron acceptance after Cu-doping.[34,35] Conversely, the Se 3d (Fig. 2g) and C 1s (Fig. S5†) in Cu-Co$_{0.85}$Se@NC move towards the high binding energy direction, indicating electron depletion after Cu doping.[29] However, the N 1s peak (Fig. S6†) does not show a significant change, indicating that electron transfer primarily takes place between Cu-Co$_{0.85}$Se and carbon. The carbon in two composite materials was further characterized by Raman spectroscopy (Fig. 2h). The D-band and G-band peaks at 1328 and 1565 cm^{-1}, respectively, are distinctive features of carbonaceous materials, suggesting the presence of amorphous carbon in the composites.[36] Additionally, the Raman peaks of Cu-Co$_{0.85}$Se@NC shifted to higher wavenumbers compared to Co$_{0.85}$Se@NC, indicating that carbon is in an electron-deficient state.[37] The electronic interaction between Cu-Co$_{0.85}$Se and carbon provides favorable possibilities for optimizing electrocatalytic performance.

Linear sweep voltammetry (LSV) was used to evaluate the hydrogen evolution performance of Co$_{0.85}$Se@NC and Cu-Co$_{0.85}$Se@NC. The hydrogen evolution polarization curves in Fig. 3a revealed onset overpotentials of 185 mV for Co$_{0.85}$Se@NC and 70 mV for Cu-Co$_{0.85}$Se@NC. In addition, Cu-Co$_{0.85}$Se@NC needed only 208 mV to reach a current density of 10 mA cm^{-2}, while the Co$_{0.85}$Se@NC electrocatalyst required a higher overpotential of 272 mV. Tafel slopes (Fig. 3b) of 162 and 173 mV dec^{-1} were calculated for Cu-Co$_{0.85}$Se@NC and Co$_{0.85}$Se@NC, respectively, which verifies that Cu-Co$_{0.85}$Se@NC has fast hydrogen evolution kinetics. Hydrogen evolution long-term stability is executed with multi-current steps (ISTEP) measurements for the Cu-Co$_{0.85}$Se@NC catalyst. The potential of Cu-Co$_{0.85}$Se@NC electrocatalyst exhibits steady in each cycle (Fig. S7a†). In addition, its polarization curve demonstrated the superior durability of the Cu-Co$_{0.85}$Se@NC catalyst (Fig. S7b†). XRD characterization (Fig. S8†) shows that the phase composition of the Cu-Co$_{0.85}$Se@NC electrode is still preserved after the HER stability measurement, indicating its excellent stability. Additionally, Cu-Co$_{0.85}$Se@NC requires an overpotential of 189 mV to reach a current density of 10 mA cm^{-2} in comparison to 305 mV for Co$_{0.85}$Se@NC in the case of OER (Fig. 3c).

Fig. 3d demonstrates the improved oxygen production capabilities of Cu-Co$_{0.85}$Se@NC, supported by a lower Tafel

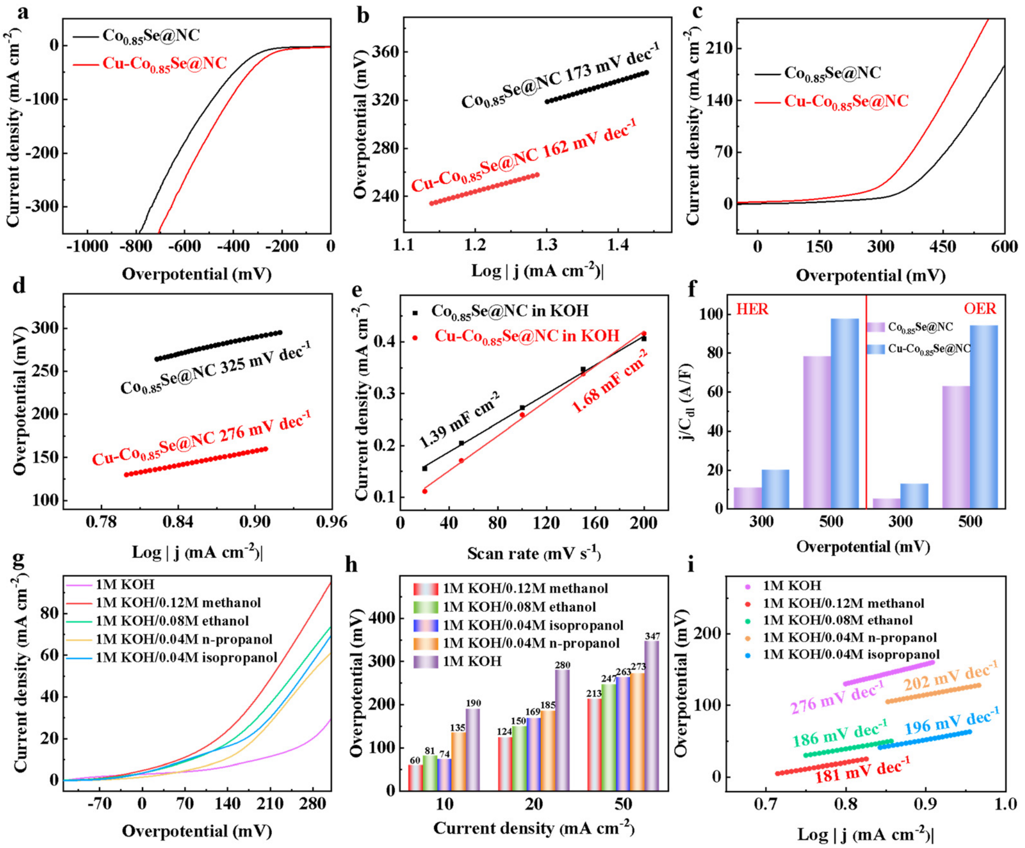

Fig. 3 (a) HER LSV curves, (b) HER Tafel slopes, (c) OER LSV curves, (d) OER Tafel slopes of Co$_{0.85}$Se@NC and Cu-Co$_{0.85}$Se@NC. (e) Plots of the capacitive currents as a function of scan rate for Co$_{0.85}$Se@NC and Cu-Co$_{0.85}$Se@NC electrodes. (f) Comparison of j/C_{dl} between Co$_{0.85}$Se@NC and Cu-Co$_{0.85}$Se@NC, where j represents the current density at a fixed overpotential. (g) LSV curves, (h) performance comparison, and (i) Tafel slopes of Cu-Co$_{0.85}$Se@NC in 1.0 M KOH with and without alcohol solvents.

slope (276 mV dec^{-1}) in comparison to Co$_{0.85}$Se@NC (325 mV dec^{-1}), suggesting better oxygen generation rates in Cu-Co$_{0.85}$Se@NC. Besides, we conducted tests to evaluate the electrochemical performance of catalysts with varying levels of copper doping (Fig. S9†). LSV curves demonstrate that Cu-Co$_{0.85}$Se@NC displays the best HER and OER properties compared to other Cu-doped catalysts, requiring low overpotentials of 208 mV and 189 mV at a current density of 10 mA cm^{-2}. Also, the Tafel slope of Cu-Co$_{0.85}$Se@NC displays smaller values of 162 mV dec^{-1} for the HER and 276 mV dec^{-1} for the OER, respectively. This indicates faster reaction kinetics for the HER and OER on the Cu-Co$_{0.85}$Se@NC catalyst compared to other Cu-doped catalysts.

The double-layer capacitances (C_{dl}) were executed to estimate the ECSA (Fig. S10† and 3e), which suggested the number of active centers.[38,39] The Cu-Co$_{0.85}$Se@NC exhibited a C_{dl} value of 1.68 mF cm^{-2}, surpassing that of Co$_{0.85}$Se@NC (1.39 mF cm^{-2}), indicating that the Cu-doped nanostructure catalyst had a greater ECSA. The ECSA of Cu-Co$_{0.85}$Se@NC is increased, which may be due to the introduction of larger-radius copper, leading to a more open nanostructure and abundantly exposed catalytic sites.[40,41] In addition, we standardized the current density (j) of an electrocatalyst by its C_{dl} to remove the impact of ECSA on electrocatalytic performance. The calculated j/C_{dl} was directly linked to the surface area-specific activity of the catalyst. The analysis shows that the j/C_{dl} of Co$_{0.85}$Se@NC is lower than that of Cu-Co$_{0.85}$Se@NC (Fig. 3f), indicating that the improved electrocatalytic efficiency of Cu-Co$_{0.85}$Se@NC is not only due to a larger active surface area but also to an increased intrinsic activity of each electrocatalytic site resulting from Cu-doping.[42] Additionally, the Nyquist curve was used in electrochemical impedance spectroscopy (EIS) measurements to determine the charge-transfer resistance (R_{ct}) in order to further analyze the reaction kinetics. As illustrated in Fig. S11,† a smaller R_{ct} was observed for Cu-Co$_{0.85}$Se@NC, which is accountable for its fast kinetics and enhanced electrocatalytic activity. Therefore, the improved catalytic property of Cu-Co$_{0.85}$Se@NC for both OER and HER can be attributed to its large ECSA, high j/C_{dl}, and small R_{ct}.

Although the overpotential of OER on Cu-Co$_{0.85}$Se@NC decreases when compared with that of Co$_{0.85}$Se@NC, the larger triggering potential still gives rise to high energy consumption. Thus, an anodic mono-alcohol oxidation reaction (M-AOR) is used as a substitute for the OER. Fig. S12† depicts the polarization curves of methanol, ethanol, isopropanol, and *n*-propanol oxidation on the Cu-Co$_{0.85}$Se@NC electrode. It is obvious that the optimal concentrations for methanol, ethanol, isopropanol, and *n*-propanol oxidation are 0.12 M, 0.08 M, 0.04 M, and 0.04 M, respectively. Besides, adding alcohol to the KOH electrolyte surprisingly reduces the overpotential on the Cu-Co$_{0.85}$Se@NC electrode (Fig. 3g). The activity order of alcohol oxidation on the Cu-Co$_{0.85}$Se@NC electrode is methanol > ethanol > isopropanol > *n*-propanol. It is conspicuous that the overpotentials of methanol oxidation at corresponding current densities are smaller than those of ethanol, *n*-propanol, and isopropanol oxidation on the Cu-Co$_{0.85}$Se@NC electrode (Fig. 3h). The reaction kinetics for methanol, ethanol, *n*-propanol, and isopropanol oxidation in alkaline electrolytes on the Cu-Co$_{0.85}$Se@NC electrode are also ascertained by the Tafel plots. The Tafel slope (Fig. 3i) of Cu-Co$_{0.85}$Se@NC was calculated to be 181 mV dec^{-1} in 0.12 M methanol, showing a decrease compared to 0.08 M ethanol (186 mV dec^{-1}), 0.04 M isopropanol (196 mV dec^{-1}) and 0.04 M *n*-propanol (202 mV dec^{-1}). The methanol oxidation on the Cu-Co$_{0.85}$Se@NC electrode exhibits the fastest reaction kinetics. The introduction of methanol led to an increase in the C_{dl} value from 1.68 to 1.83, indicating that the Cu-Co$_{0.85}$Se@NC electrode possesses a greater number of active sites for enhancing the methanol oxidation process (Fig. S13†). Additionally, the stability of methanol oxidation on the Cu-Co$_{0.85}$Se@NC electrode was measured using ISTEP measurements. As shown in Fig. S14a,† the potential for Cu-Co$_{0.85}$Se@NC depicted a slight change. The LSV curves display negligible differences compared with the initial ones (Fig. S14b†), demonstrating their superior long-term durability.

Raman spectroscopy (Fig. S15†) was conducted to evaluate the water activation and adsorption after HER in an alkaline electrolyte. The peak observed at around 500 cm^{-1} in the Raman spectrum is likely due to the vibration of the Cu–O–H bond from water molecules adsorbed on the surface of the electrocatalyst.[43] The strength of the Cu–O–H bond in Co$_{0.85}$Se@NC is noticeably lower than in Cu-Co$_{0.85}$Se@NC, indicating that the Volmer step kinetics are enhanced and water activation is more easily achieved on the surface of Cu-Co$_{0.85}$Se@NC. Additionally, the hydrophilic properties of the catalysts were evaluated as hydrophilicity is a critical factor in determining the accessibility of water to the electrocatalyst interface. The water contact angle of Co$_{0.85}$Se@NC is 51° (Fig. 4a), which is larger than that of Cu-Co$_{0.85}$Se@NC (37°, Fig. 4b). This implies that Cu-Co$_{0.85}$Se@NC is beneficial to water affinity, which is critical for facilitating the HER.[44–46] It is common knowledge that water molecules consist of two positively charged H atoms and one negatively charged O atom; electron modulation endows positively charged Cu in composite materials with the ability to adsorb and activate water molecules by fixing the oxygen atom of water, thereby enhancing the hydrophilicity of Cu-Co$_{0.85}$Se@NC.[27]

Furthermore, to investigate the impact of molecular species on alcohol oxidation reaction performance, contact angle measurements were also conducted for methanol, ethanol, isopropanol, and *n*-propanol molecules adsorbed on Cu-Co$_{0.85}$Se@NC catalyst. Fig. 4c and S16† depict the test results, from which it can be obviously identified that the contact angle of methanol onto Cu-Co$_{0.85}$Se@NC (11°) is lower than that of ethanol (16°), isopropanol (21°), and *n*-propanol (26°), indicating that the methanol has an optimum adsorption characteristic, which in turn proves that methanol oxidation possesses the highest activity on Cu-Co$_{0.85}$Se@NC electrode in alkaline electrolyte.[47–49] Based on the above analysis, Fig. 4d systematically displays the possible mechanism of superior methanol oxidation reaction (MOR) and HER activities for Cu-Co$_{0.85}$Se@NC electrocatalyst, where cobalt selenide serves as an

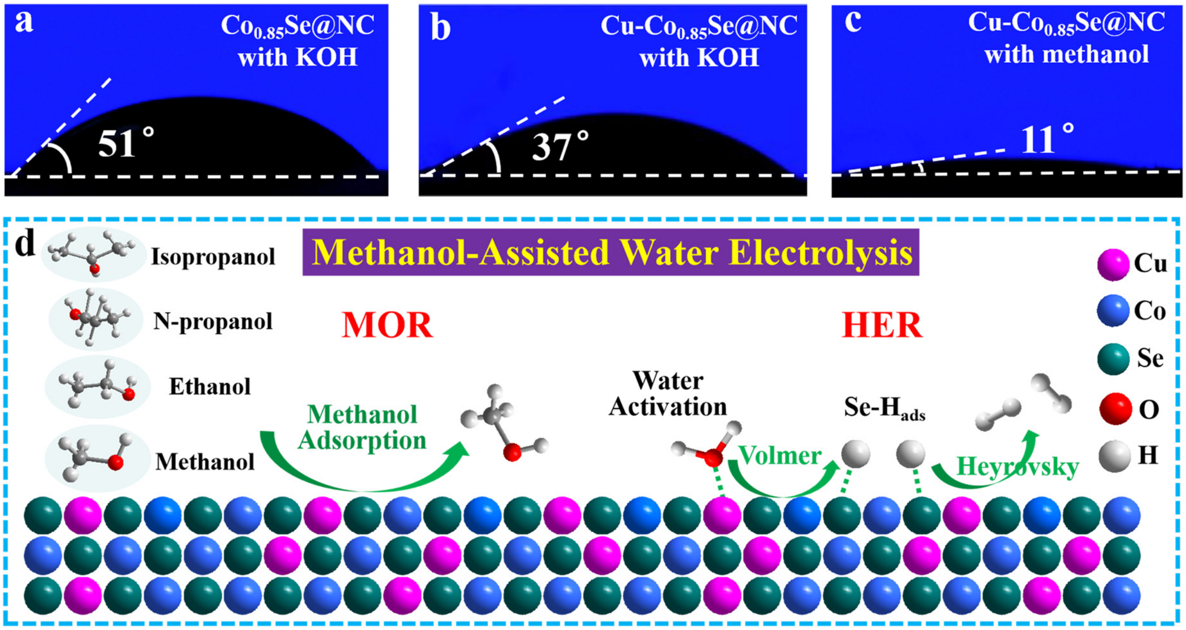

Fig. 4 The contact angles of (a) $Co_{0.85}Se$@NC and (b) Cu-$Co_{0.85}Se$@NC in 1.0 M KOH. (c) The contact angle of Cu-$Co_{0.85}Se$@NC in methanol. (d) Schematic illustration of MOR and HER mechanisms for Cu-$Co_{0.85}Se$@NC catalyst.

acceptor of methanol and atomic copper substantially adsorbs H_2O molecules, thus facilitating the excellent catalytic property for MOR and HER simultaneously.

As previously mentioned, the as-synthesized Cu-$Co_{0.85}Se$@NC displays superior electrocatalytic properties for HER and M-AOR, which could be attributed to the following aspects: (i) the pores of MOF-derived materials are conducive to liberating the formed gases and facilitating close contacts between electrolytes and active sites; (ii) the N-doped carbon framework is beneficial for promoting charge transfer and enhancing electrode reaction kinetics, while simultaneously preventing catalyst corrosion and improving its long-term stability; (iii) Cu-doping can effectively regulate the electronic structure of cobalt selenide, optimize its adsorption on reactants (or intermediates), and thereby improve the intrinsic activity of cobalt selenide. Based on the excellent catalytic performance of HER and MOR, Cu-$Co_{0.85}Se$@NC was used as a bifunctional catalyst in a methanol–water electrolysis configuration. Fig. 5a shows that in a methanol–water system, achieving current densities of 10 and 50 mA cm^{-2} requires driving voltages of 1.46 V and 1.75 V, respectively. In conventional water electrocatalysis systems, higher driving voltages (1.76 V and 2.01 V) are required, demonstrating the superior efficiency of methanol–water

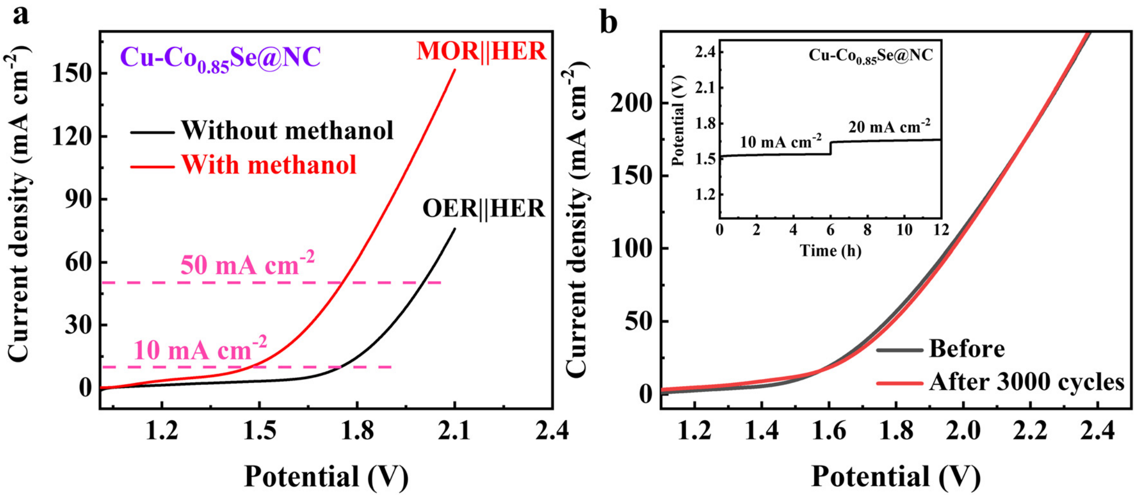

Fig. 5 (a) Cell LSV curve comparison of water electrolysis and methanol–water electrolysis using Cu-$Co_{0.85}Se$@NC as anode and cathode in KOH with and without methanol. (b) LSV curves of Cu-$Co_{0.85}Se$@NC before and after the stability test (the inset is the stability test of Cu-$Co_{0.85}Se$@NC).

electrolysis. The electrolyzer displayed almost the same electrocatalytic properties after the stability test (Fig. 5b). Besides, we also evaluated the stability of the catalyst through *i*–*t* measurements. As shown in Fig. S17,† the fluctuation of the *i*–*t* curve is small, which further indicates the excellent stability of the Cu-$Co_{0.85}Se$@NC catalyst. Therefore, in view of the MOR and HER catalytic activity and durability, the as-prepared Cu-$Co_{0.85}Se$@NC could be a promising bifunctional electrocatalyst for methanol–water electrolysis.

4. Conclusions

In summary, a Cu-doped cobalt selenide@nitrogen-doped carbon composite was successfully synthesized. The electronic structure of cobalt selenide is regulated by controllable Cu-doping to significantly improve its electrocatalytic properties. As a result, the required overpotentials for achieving a current density of 10 mA cm^{-2} in the MOR and HER were determined to be only 56 mV and 208 mV, respectively. Moreover, the Cu-$Co_{0.85}Se$@NC catalyst was used as both the anode and cathode in a two-electrode electrolytic cell, requiring a voltage of 1.46 V to achieve a current density of 10 mA cm^{-2}, which was significantly less than the voltage needed for the conventional water splitting system. This work offers an effective method to fabricate high-performance catalysts for methanol-assisted H_2 evolution by integrating MOR/HER active sites into Cu-doped cobalt selenide composites.

Data availability

The data that support the findings of this study are available from the corresponding author upon reasonable request.

Author contributions

Lei Hu: writing – original draft, funding acquisition, supervision. Peng Zhong: writing – original draft, investigation. Jie Zhu: investigation, formal analysis. Jiacheng Wang: project administration. Yuchen Zheng: data curation. Xiaoming Lin: conceptualization. Yuyang Zhang: data curation. Hao Yang: project administration, supervision.

Conflicts of interest

All authors declared that there are no conflicts of interest.

Acknowledgements

This work was supported by the Scientific Research Project of Anhui Polytechnic University for Undergraduates (2023DZ23), Anhui Province Action Plan for Cultivating Middle and Young Teachers (YQZD2023042), and the National Training Program of Innovation and Entrepreneurship for Undergraduates (202310363065). The authors express their gratitude to Qian Wang from SCI-GO (**https://www.sci-go.com**) for conducting the XPS test.

References

1 Y. He, Y. Hu, Z. Zhu, J. Li, Y. Huang, S. Zhang, M. S. Balogun and Y. Tong, *Chem. Eng. J.*, 2024, **489**, 151348.
2 Z. Lu, H. Yang, Q. Liu, J. Luo, L. Feng, L. Chu and X. Liu, *Small*, 2024, **20**, 2305434.
3 Q. Qian, Y. Zhu, N. Ahmad, Y. Feng, H. Zhang, M. Cheng, H. Liu, C. Xiao, G. Zhang and Y. Xie, *Adv. Mater.*, 2024, **36**, 2306108.
4 R. Li, K. Xiang, Z. Peng, Y. Zou and S. Wang, *Adv. Energy Mater.*, 2021, **11**, 2102292.
5 S. Behera, S. Ganguly, C. Loha, B. Mondal and S. Ghosh, *Energy Fuels*, 2023, **37**, 7603–7633.
6 J. Hao, J. Liu, D. Wu, M. Chen, Y. Liang, Q. Wang, L. Wang, X.-Z. Fu and J.-L. Luo, *Appl. Catal., B*, 2021, **281**, 119510.
7 X. Wei, S. Wang, Z. Hua, L. Chen and J. Shi, *ACS Appl. Mater. Interfaces*, 2018, **10**, 25422–25428.
8 S. Sheng, K. Ye, L. Sha, K. Zhu, Y. Gao, J. Yan, G. Wang and D. Cao, *Inorg. Chem. Front.*, 2020, **7**, 4498–4506.
9 F. Arshad, T. u. Haq, I. Hussain and F. Sher, *ACS Appl. Energy Mater.*, 2021, **4**, 8685–8701.
10 T. Wu, X. Zhu, G. Wang, Y. Zhang, H. Zhang and H. Zhao, *Nano Res.*, 2017, **11**, 1004–1017.
11 Q. Zhang, G. Zhang, S. Guan, J. Wang, K. Li, C. Wang and T. Guan, *J. Colloid Interface Sci.*, 2024, **662**, 686–694.
12 N. Abdullah, R. Saidur, A. M. Zainoodin and N. Aslfattahi, *J. Cleaner Prod.*, 2020, **277**, 123395.
13 N. A. I. Md Ishak, S. K. Kamarudin, M. Mansor, N. Yahya, R. Bahru and S. Rahman, *J. Cleaner Prod.*, 2024, **440**, 140637.
14 F. Wang, Y. Li, T. A. Shifa, K. Liu, F. Wang, Z. Wang, P. Xu, Q. Wang and J. He, *Angew. Chem., Int. Ed.*, 2016, **55**, 6919–6924.
15 W. Feng, W. Pang, Y. Xu, A. Guo, X. Gao, X. Qiu and W. Chen, *ChemElectroChem*, 2020, **7**, 31–54.
16 X. Peng, Y. Yan, X. Jin, C. Huang, W. Jin, B. Gao and P. K. Chu, *Nano Energy*, 2020, **78**, 105234.
17 Q. Huang, X. Liu, Z. Zhang, L. Wang, B. Xiao and Z. Ao, *Chin. Chem. Lett.*, 2023, **34**, 108046.
18 X. Xia, L. Wang, N. Sui, V. L. Colvin and W. W. Yu, *Nanoscale*, 2020, **12**, 12249–12262.
19 X. Zhao, X. Li, Y. Yan, Y. Xing, S. Lu, L. Zhao, S. Zhou, Z. Peng and J. Zeng, *Appl. Catal., B*, 2018, **236**, 569–575.
20 M. Mekete Meshesha, D. Chanda, S. Gwon Jang and B. Lyong Yang, *Chem. Eng. J.*, 2023, **474**, 145708.
21 X. Zhang, X. Gao, R. Han, S. Wang, M. Liu, Q. Lu and E. Guo, *J. Electroanal. Chem.*, 2023, **950**, 117897.
22 J. Ding, H. Yang, H. Zhang, Z. Wang, Q. Liu, L. Feng, G. Hu, J. Luo and X. Liu, *Int. J. Hydrogen Energy*, 2024, **53**, 318–324.
23 Y. Liu, Z. Tian, Q. Xu, Y. Yang, Y. Zheng, H. Pan, J. Chen, Z. Wang and W. Zheng, *ACS Appl. Mater. Interfaces*, 2022, **14**, 8963–8973.
24 X. Cao, J. E. Medvedeva and M. Nath, *ACS Appl. Energy Mater.*, 2020, **3**, 3092–3103.
25 J. Dai, D. Zhao, W. Sun, X. Zhu, L.-J. Ma, Z. Wu, C. Yang, Z. Cui, L. Li and S. Chen, *ACS Catal.*, 2019, **9**, 10761–10772.
26 P. Liu, Y. Liu, K. Wang, S. Shi, M. Jin, J. Liu, T. Qin, Q. Liu, X. Liu and J. He, *Nano Res.*, 2024, **17**, 4797.

27 L. Hu, P. Zhong, X. Zhang, Y. Xiang, M. S. Balogun, Y. Tong and H. Yang, *Appl. Surf. Sci.*, 2023, **623**, 157040.

28 L. Hu, Y. Hu, R. Liu, Y. Mao, M. S. Balogun and Y. Tong, *Int. J. Hydrogen Energy*, 2019, **44**, 11402–11410.

29 R. Banerjee, A. Phan, B. Wang, C. Knobler, H. Furukawa, M. O'Keeffe and O. M. Yaghi, *Science*, 2008, **319**, 939–943.

30 L. Hu, L. Li, Y. Zhang, X. Tan, H. Yang, X. Lin and Y. Tong, *J. Mater. Sci. Technol.*, 2022, **127**, 124–132.

31 L. Jiao, Y. Luo and L. Cheng, *Colloids Surf., A*, 2023, **664**, 131122.

32 R. Deng, Q. Li, P. Wang, Q. Zheng, Y. Huo, F. Xie and D. Lin, *Electrochim. Acta*, 2022, **432**, 141157.

33 Y. Wang, S. Li, D. Zhang, F. Tan, L. Li and G. Hu, *J. Alloys Compd.*, 2021, **889**, 161696.

34 Z. Xue, X. Li, Q. Liu, M. Cai, K. Liu, M. Liu, Z. Ke, X. Liu and G. Li, *Adv. Mater.*, 2019, **31**, 1900430.

35 Z. Xue, Y. Li, Y. Zhang, W. Geng, B. Jia, J. Tang, S. Bao, H.-P. Wang, Y. Fan, Z.-w. Wei, Z. Zhang, Z. Ke, G. Li and C.-Y. Su, *Adv. Energy Mater.*, 2018, **8**, 1801564.

36 A. C. Ferrari and J. Robertson, *Phys. Rev. B: Condens. Matter Mater. Phys.*, 2000, **61**, 14095–14107.

37 L. Yang, R. Grzeschik, P. Jiang, L. Yu, C. Hu, A. Du, S. Schlücker and W. Xie, *Angew. Chem., Int. Ed.*, 2023, **62**, e202301065.

38 Y. Chen, X. Li, H. Yang and Y. Huang, *Small*, 2024, 2402406.

39 Y. Wang, J. Huang, Y. Chen, H. Yang, K.-H. Ye and Y. Huang, *J. Colloid Interface Sci.*, 2024, **672**, 12–20.

40 I. U. Islam, Y. Zhang, A. Iqbal, J. Zai, A. Waseem and X. Qian, *Electrochim. Acta*, 2024, **485**, 144111.

41 Y. Wang, Y. Chen, Y. Yun, X. Hong, Y. Huang and H. Ji, *Appl. Catal., B*, 2024, **358**, 124375.

42 G. Zhang, Y.-S. Feng, W.-T. Lu, D. He, C.-Y. Wang, Y.-K. Li, X.-Y. Wang and F.-F. Cao, *ACS Catal.*, 2018, **8**, 5431–5441.

43 S. Anantharaj, H. Sugime and S. Noda, *ACS Appl. Mater. Interfaces*, 2020, **12**, 27327–27338.

44 B. K. Kim, M. J. Kim and J. J. Kim, *ACS Appl. Mater. Interfaces*, 2021, **13**, 11940–11947.

45 W. He, R. Zhang, D. Cao, Y. Li, J. Zhang, Q. Hao, H. Liu, J. Zhao and H. L. Xin, *Small*, 2023, **19**, 2205719.

46 H. Zheng, F. Yang, T. Xiong, D. Adekoya, Y. Huang and M. S. J. T. Balogun, *ACS Appl. Mater. Interfaces*, 2020, **12**, 57093–57101.

47 Y. Yang, D. Xu, B. Zhang, Z. Xue and T. Mu, *Chem. Eng. J.*, 2022, **433**, 133842.

48 G. Zhao, F. Yang, Z. Chen, Q. Liu, Y. Ji, Y. Zhang, Z. Niu, J. Mao, X. Bao, P. Hu and Y. Li, *Nat. Commun.*, 2017, **8**, 14039.

49 M. Li, P. Liu and R. R. Adzic, *J. Phys. Chem. Lett.*, 2012, **3**, 3480–3485.